Bridging Large-Signal and Small-Signal Responses of Hafnium-Based Ferroelectric Tunnel Junctions

Bridging Large-Signal and Small-Signal Responses of Hafnium-Based Ferroelectric Tunnel Junctions

M. Massarotto[1], M. Segatto[1], F. Driussi[1], A. Affanni[1], S. Lancaster[2], S. Slesazeck[2], T. Mikolajick[2,3], D. Esseni[1]

[(1)]DPIA, University of Udine, Udine, Italy; [(2)]NaMLab gGmbH, Dresden, Germany; [(3)]Chair of Nanoelectronics, IHM, TU–Dresden, Germany.

Abstract

Ferroelectric Tunnel Junctions (FTJs) operating as memristors are promising electron devices to realize artificial synapses for neuromorphic computing. But the understanding of their operation requires an in-depth electrical characterization. In this work, an in-house experimental setup is employed along with novel experimental methodologies to investigate the large-signal (LS) and small-signal (AC) responses of FTJs. For the first time, our experiments and physics-based simulations help to explain the discrepancies between LS and AC experiments reported in previous literature.

Index Terms

Ferroelectric, Hafnium Zirconium Oxide (HZO), Ferroelectric Tunnel Junction (FTJ), Experimental Characterization, Small Signal Analysis

 DOI: 10.1109/ICMTS55420.2023.10094178

I. Introduction

In recent years, HfO_2-based Ferroelectric Tunnel Junctions (FTJs) with a Metal-Ferroelectric-Dielectric-Metal (MFDM) structure have been proposed and investigated as energy-efficient synapses for neuromorphic computing [1], [2]. Nevertheless, the optimization of ferroelectric (FE) devices, such as the FTJs, requires a comprehensive understanding of their operation, particularly to evaluate the complex trade-offs involving stored polarization, trapped charge in the dielectric stack and read current [3]. Unfortunately, standard measurement techniques appear to fail to completely uncover the physical mechanisms behind the FTJs

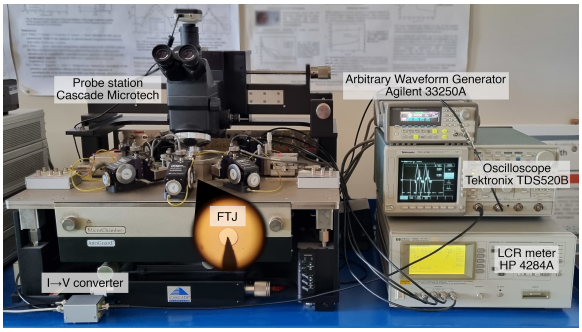

Figure 1: Photograph of our experimental setup dedicated to the characterization of FTJs. The circular FTJs under test (central inset) have a diameter ranging from 110 µm to 450 µm and are measured directly on Si wafers through the Cascade Microtech probe station.

electrical operation; for instance, the measured small-signal (AC) capacitance cannot be easily correlated to the quasi-static characteristics of the FTJs [4]. In fact, the FE spontaneous polarization plays a significant role in the FTJs quasi-static response, while it is much less prominent in AC measurements, puzzling the interpretation of the experimental results [5]–[7].

In this respect, we developed a versatile experimental setup (see Figs. 1 and 2) able to perform both quasi-static characterizations (large signals, LS, at low frequencies) [8], and conventional AC analyses (at medium–high frequencies) [9] of FTJs. Our versatile setup confirmed the quantitative disagreement between the LS and AC responses of the FTJs and, for this reason, in this work we have made extensive use of the new electrical characterization procedure first presented in [9], providing a bridge between the LS and AC experiments. Furthermore, the interpretation of such novel results is also supported by physics-based modeling [3].

II. Device fabrication

We fabricated the MFDM FTJs (see Fig. 2) by depositing 10 nm $Hf_{0.5}Zr_{0.5}O_2$ (HZO) and 2 nm Al_2O_3 on top of W (30 nm)/TiN (10 nm) bottom electrodes via Atomic Layer Deposition (ALD). The top contacts (MD) consist of a 10 nm TiN layer deposited by reactive sputtering under ultra-high vacuum. In order to stabilize the ferroelectric phase, a crystallization anneal was performed at 500 °C for 20 s. Finally, capacitors are defined by depositing Ti (10 nm)/Pt (25 nm) through a shadow mask, used for SC-1 etching of the TiN layer.

III. Developed experimental setup

Our versatile, in-house-developed experimental setup for the characterization of FTJs is portrayed and sketched in Figs. 1 and 2, respectively. In particular, an Agilent 33250A Arbitrary Waveform Generator issues the input voltage V_{IN} which drives the FTJ under test.

The switched polarization is a crucial parameter in FTJs, as it modifies the band bending and thereby determines the FTJ read current [3]. In order to inspect the polarization of the HZO layer, the switching

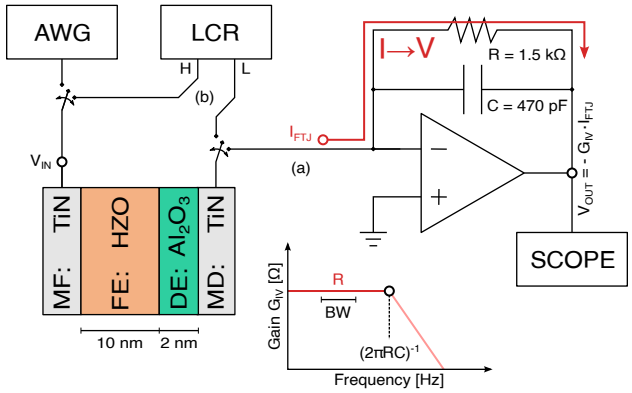

Figure 2: Sketch of the experimental setup and of the MFDM FTJs characterized in this work. (a) The Arbitrary Waveform Generator (AWG) drives the FTJ by applying V_{IN}, inducing a displacement current (I_{FTJ}) which is converted into an output voltage (V_{OUT}) thanks to the I→V converter. The switching charge Q_{FTJ} is obtained by numerical integration of the I_{FTJ} recorded by the oscilloscope. (b) The LCR meter, instead, allows for standard AC characterizations.

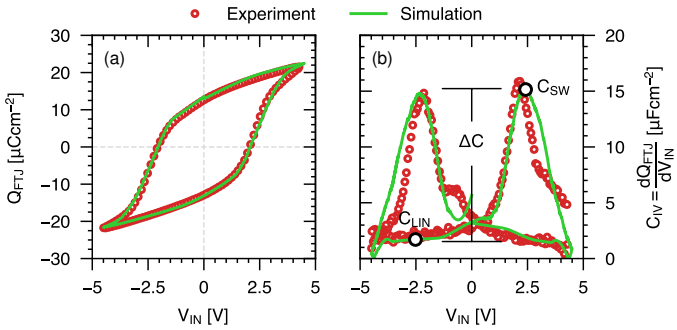

Figure 3: (a) Comparison between measured (symbols) and simulated (line) Q_{FTJ} vs. V_{IN} curves. Experimental Q_{FTJ} is typically interpreted as the total polarization of the FTJ, and here it has been obtained by integrating the I_{FTJ} measured with 10 kHz triangular pulses. (b) Simulated (line) and experimental (symbols) effective LS capacitance ($C_{IV} = \partial Q_{FTJ}/\partial V_{IN}$). The linear capacitance (C_{LIN}), the peak capacitance (C_{SW}) and the difference $\Delta C = C_{SW} - C_{LIN}$ are also defined.

current I_{FTJ} induced by a triangular V_{IN} pulse is converted by a virtual-grounded I→V converter into an output voltage V_{OUT}, which is recorded over time by a Tektronix TDS520B oscilloscope. The triangular V_{IN} pulses allow us to distinguish the I_{FTJ} peaks caused by the polarization switching from the fairly voltage-independent plateaus due to the dielectric response of the stack [9].

The measured current waveform is then numerically integrated to compute the switching charge Q_{FTJ}, thus obtaining the hysteretic Q_{FTJ}–V_{IN} characteristic of Fig. 3a. Q_{FTJ} is typically interpreted as the FTJ total polarization P, even if this is an underestimation due to the complex fields in the stack [10]. Furthermore, by differentiating the polarization w.r.t. the input voltage, an effective LS capacitance (C_{IV}) can be defined, as reported in Fig. 3b. The reliability of our setup in measuring these quasi-static characteristics has been thoroughly assessed in [8], [9].

Thanks to its versatility, our setup can also perform dedicated AC analyses. In fact, we investigated the AC response of the FTJ stack under the same experimental conditions as those used for the Q_{FTJ}–V_{IN}

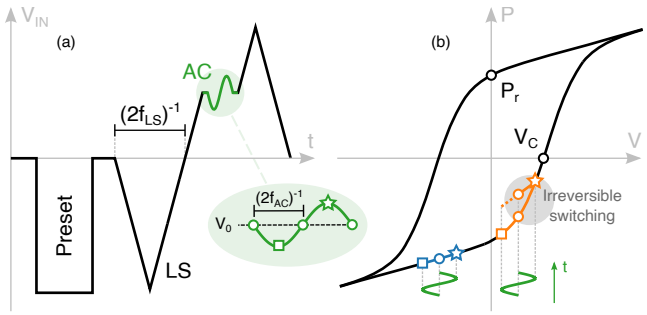

Figure 4: (a) Sketch of the AC measurement performed to mimic the LCR meter measurement. The LS triangular pulse drives the FTJ up to a given bias V_0, where the AC response is monitored by issuing a sinusoidal (or triangular, not shown) AC signal. (b) Sketch of the minor loops followed by an FTJ undergoing the AC signal when V_0 is in the linear (blue) or switching branch (orange) of the P–V_{IN} hysteresis. V_C is the positive coercive voltage of the FTJ.

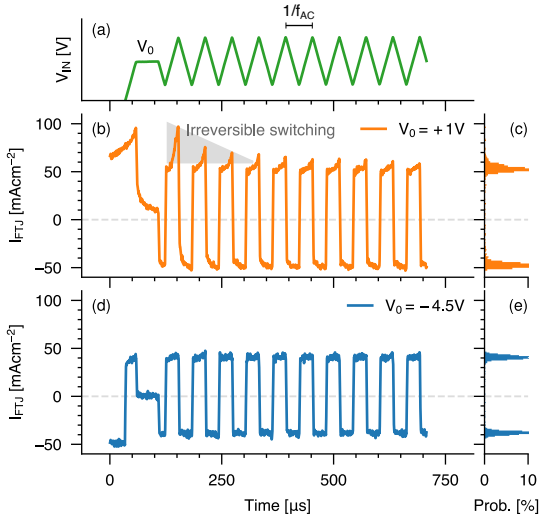

Figure 5: Experimental response of an FTJ undergoing a triangular AC excitation with $f_{AC} = 17\,\text{kHz}$. The time evolution of the applied V_{IN} (a) and of the I_{FTJ} values measured at two V_0 biases, respectively close (b) and far (d) from the coercive voltages, are shown. When V_0 is close to the coercive voltages, the measurements show traces of an irreversible polarization switching (grey area) that vanish for subsequent periods of the AC signal. (c, e) Probability histograms of I_{FTJ} used to extract the amplitude of the AC response.

curves. To do so, we employed the V_{IN} signal sketched in Fig. 4a. Here, a triangular LS pulse, akin to those used to extract the curves of Fig. 3a, drives the FTJ up to a given bias V_0, then an AC signal (sinusoidal or triangular [9]) is superimposed and the induced I_{FTJ} is measured. Figure 4b sketches the expected different behaviors of the FTJs when the bias V_0 is close or far from the stack coercive voltages $\pm V_c$.

The experimental results shown in Fig. 5 confirm that a triangular AC waveform (Fig. 5a) produces a square-wave current (Fig. 5d) when V_0 is far from $\pm V_c$, thus reflecting a purely dielectric response of the stack. On the other hand, when V_0 lies close to $\pm V_c$, I_{FTJ} exhibits also large peaks during the very first pulses (Fig. 5b). Such peaks tend to vanish in the subsequent periods, suggesting an irreversible switching of the polarization induced by the AC signal.

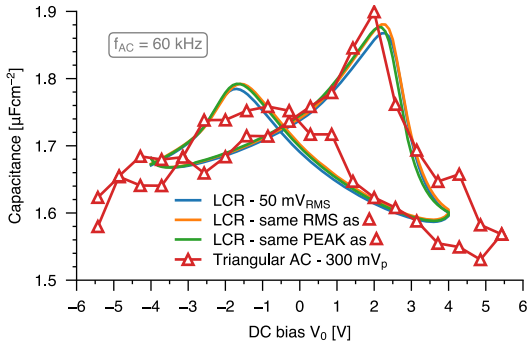

Figure 6: Comparison between the AC capacitance either extracted with our setup (red triangles) by issuing a 60 kHz/300 mV-peak AC triangular wave (same as in Fig. 5), or measured with the LCR meter by using 60 kHz sinusoidal waves. The curves measured by the LCR meter are fairly insensitive to the amplitude of the sinusoidal signal.

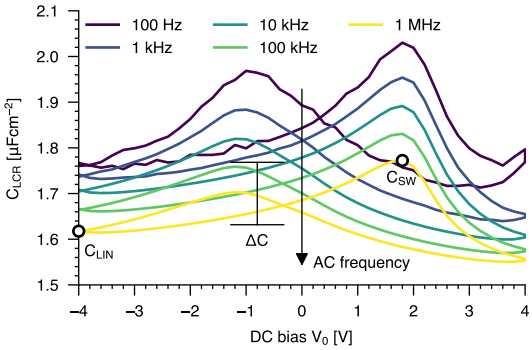

Figure 7: AC capacitance measured by the LCR meter in the 100 Hz—1 MHz range. The linear capacitance C_{LIN}, the peak capacitance C_{SW} and their difference ΔC are defined in the figure.

The AC response amplitude in Fig. 5 is then extracted from the peak positions in the I_{FTJ} probability histograms of Figs. 5c and 5e. At each V_0 bias, this value is then divided by the V_{IN} slew rate, thus obtaining the capacitance curve of Fig. 6 (symbols). This latter has been compared to standard AC measurements (C_{LCR}, Fig. 7) performed by an HP4284A LCR meter (see Fig. 2b), and their good agreement testifies to the suitability of our setup based on the arbitrary waveform generator also for AC analyses.

It is worth pointing out that the capacitance curves measured with both our *ad-hoc* procedure in Fig. 5 and the LCR meter exhibit a hysteretic "butterfly" shape with evident capacitance peaks (C_{SW}, Fig. 7) at $\pm V_c$, rising above the baseline (C_{LIN}) due to the pure dielectric response of the stack. This behavior is similar to that shown by the effective capacitance C_{IV} obtained from the LS experiments and reported in Fig. 3b. This testifies that the FE polarization not only contributes to the LS response of the FTJ but also to the measured AC capacitance. However, while in both the LS and AC regimes C_{LIN} remains almost identical, it is evident that the C_{SW} peaks in the C_{LCR} of Fig. 7 are much lower than those of C_{IV} in Fig. 3b. This has been routinely observed also in the literature [4]–[6] and it is presumably due to the fact that the irreversible polarization switching contributes to C_{IV}, while it tends to vanish during the AC pulsing, as clearly shown by Fig. 5b.

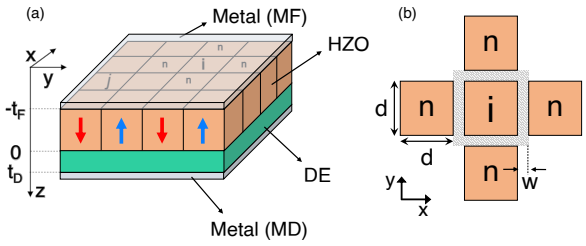

Figure 8: Sketch of the simulated MFDM stack. (a) 3D view of simulated structure, showing the HZO layer thickness t_F, the dielectric (DE) layer thickness t_D, and the partition of HZO in n_D domains. The HZO capacitance is $C_F = \varepsilon_0\varepsilon_F/t_F$ and the DE capacitance is $C_D = \varepsilon_0\varepsilon_D/t_D$. C_0 is the sum of C_F and C_D, while C_S is the capacitance of their series connection. (b) Sketch showing the domains adjacent to a generic domain i involved in the domain wall term in Eq. (1); d and w are the size and wall width of the domain [11]. LGD parameters are extracted by imposing a coercive field $E_C \simeq 1.8\,\mathrm{MV\,cm^{-1}}$ and a remnant polarization $P_r \simeq 16\,\mu\mathrm{C\,cm^{-2}}$. We used an E_C statistical dispersion with standard deviation over mean value $\sigma_{Ec} = 30\%$. Traps are deeper than 0.5 eV below the HZO conduction band at the FE–DE interface and extend over 2 eV. Trap density is $5 \cdot 10^{13}\,\mathrm{cm^{-2}\,eV^{-1}}$ and capture/emission rate is 20 kHz.

IV. Simulation framework

To interpret the experiments and to gain insight into the contribution to the LS and AC responses of FTJs due to the polarization switching, we made use of the calibrated physics-based model for MFDM stacks presented in [11]. The model relies on the Landau–Ginzburg–Devonshire (LGD) theory and includes trapping at the HZO–Al_2O_3 interface.The HZO layer is partitioned into n_D domains (Fig. 8) and the spontaneous polarization (P_i) dynamics in each domain i is modelled as [2], [3], [10], [11]:

$$\begin{aligned}\frac{\partial P_i}{\partial t} = \frac{1}{t_F\,\rho}[&-\left(2\alpha_i\,P_i + 4\beta_i\,P_i^3 + 6\gamma_i\,P_i^5\right)t_F \\ &- \frac{t_F\,k}{d\,w}\sum_n\left(P_i - P_n\right) - \sum_{j=1}^{n_D}\left(P_j + Q_{T,j}\right)/C_{i,j} \\ &+ (C_D/C_0)V_{IN}]\end{aligned} \tag{1}$$

where the j index indicates the generic domain in the grid of Fig. 8a, while the n index runs over the domains adjacent to the i-th domain. The domain-dependent LGD coefficients α_i, β_i and γ_i follow from a normal distribution of coercive fields, with the parameters reported in the caption of Fig. 8; k is the domain wall coupling factor which accounts for the domain wall energy; ρ is the domain viscosity or switching resistivity and $C_{i,j}$ describes the capacitive coupling between the i-th and j-th domains. In all simulations, we set $k \approx 0$ according to first-principle calculations [12], and $\rho = 110\,\Omega\,\mathrm{m}$ corresponding to a characteristic switching time $t_\rho = \rho/(2\alpha_{mean}) \simeq 40\,\mathrm{ns}$, in accordance with ultra-fast switching measurements in HZO [13]. All the reported results are for $n_D = 100$ and we verified that increasing n_D does not produce any significant change in the results. The trapping dynamics are governed by a first-order differential equation for the electron density $n_{Tr,i}$ inside the traps at the HZO–Al_2O_3 interface at the energy E_T [3], [10]:

$$\frac{\partial n_{Tr,i}(E_T)}{\partial t} = \left[N_T(E_T) - n_{Tr,i}(E_T)\right]c_n - n_{Tr,i}(E_T)e_n \tag{2}$$

where c_n and e_n are the capture and emission rates, respectively [3], [10], [14], while $N_T(E_T)$ is the interface trap density at the trap energy E_T.

The ferroelectric and trapping dynamics are solved self-consistently, and from $n_{Tr,i}$ the total trapped charge per unit area is readily calculated as:

$$\begin{aligned} Q_{T,i} = &- q \sum_{E_T,acc} n_{Tr,i}(E_{T,acc}) \\ &+ q \sum_{E_T,don} [N_{T,don}(E_{T,don}) - n_{Tr,i}(E_{T,don})] \end{aligned} \tag{3}$$

where $E_{T,acc}$ and $E_{T,don}$ denote the energies for the acceptor and donor traps, respectively.

The LS simulations agree quite well with the experiments (Fig. 3), confirming the validity of the simulation framework. Therefore, we used this model to also simulate the FTJ response to arbitrary input signals. Simulations are then compared to the measurements performed with our setup to gain insight into the FE dynamics when the FTJ is operated in both the LS and AC regimes. The results are reported in the next section.

V. Measurements and simulations to bridge LS and AC responses of FTJs

In order to better investigate the large difference in the LS and AC peaks (C_{SW}) evidenced by the comparison of Figs. 3b and 7 in Section III, we leveraged the versatility of our setup by devising a novel characterization technique able to simultaneously probe both the LS and AC responses of the FTJs. To do that, we superimpose an AC sinusoidal wave (V_{AC}, with amplitude A_{AC} and frequency f_{AC}) to a triangular LS pulse (V_{LS}, with amplitude $A_{LS} \gg A_{AC}$ and frequency f_{LS}), thus obtaining the composite waveform sketched in Fig. 9a.

The induced I_{FTJ} (Fig. 9b) exhibits sinusoidal fluctuations on top of an LS component (dashed line), that resemble the FTJ current induced also by triangular pulses [9]. The spectrum of I_{FTJ} in Fig. 10 suggests that for $f_{LS} \ll f_{AC}$, the LS and AC components can be separated in post-processing via low-pass and band-pass numeric filters, respectively. In particular, in order to obtain the AC current component I_{AC}, we have used a filter with a bandwidth equal to $60 \times f_{LS}$ centered around f_{AC}. This choice is supported by the fact that the extracted I_{AC} in Fig. 9c behaves like an AM-modulated sinusoidal carrier of frequency f_{AC}, as it is confirmed also by the double-sided shape around f_{AC} of its spectrum in Fig. 10.

Once I_{AC} has been obtained, the AC capacitance can be readily computed as $C_{AC} = |I_{AC}|/2\pi f_{AC} A_{AC}$, whose envelope (Fig. 9d) resembles the AC capacitance of Figs. 6 and 7. In particular, far from the switching peaks, the obtained C_{AC} shows the expected C_{LIN} value of the stack, thus verifying the reliability of this procedure to evaluate the AC response of the FTJs.

By following a similar procedure, the LS component (I_{LS}, Fig. 9b, dashed line) of I_{FTJ} has been extracted via an ideal low-pass filter of bandwidth $B_{LS} = 30 \times f_{LS}$. Then, the LS capacitance is calculated as $C_{LS} = |I_{LS}|/(\partial V_{LS}/\partial t) = |I_{LS}|/(4 f_{LS} A_{LS})$, whose values are identical to those in Fig. 3b (see Fig. 9f), proving again the validity of the filtering procedure.

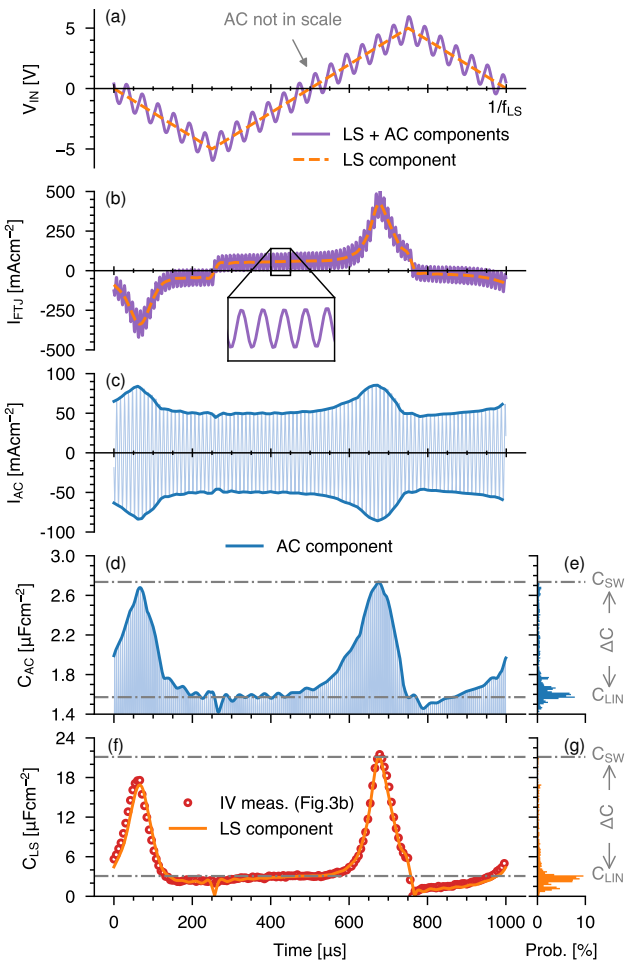

Figure 9: Combined LS/AC measurements: (a) V_{IN} (purple) is the superimposition of a triangular pulse ($f_{LS} = 1\,\text{kHz}$, dashed orange) and a sinusoidal waveform ($f_{AC} = 100\,\text{kHz}$). (b) The resulting I_{FTJ} (purple) shows sinusoidal fluctuations (inset) superimposed on the LS component (dashed orange). (c) AC current extracted by filtering I_{FTJ}. (d) AC capacitance computed from the AC current. (f) LS capacitance calculated from the LS component of I_{FTJ} [dashed orange in (b)]. The excellent agreement between C_{LS} and C_{IV} from Fig. 3b validates the filtering method. (e, g) Probability histograms of the C_{AC} envelope [darker line of (d)] and of C_{LS}. Histograms are used to obtain C_{LIN}, C_{SW} and their difference ΔC.

The V_{IN} waveform in Fig. 9a and the post-processing procedure to separate the LS and AC responses have been used also for simulations, so as to closely emulate the experimental conditions. Figure 11a shows the good qualitative agreement between the simulations and the experiments, which legitimates the use of the model to gain additional insights into the physical mechanisms involved in the FTJ response to such a complex driving stimulus.

By denoting with Q_{MF} the charge at the MF electrode (see Fig. 8) we can write [10]:

$$Q_{MF} = \frac{C_D}{C_0} P_{AV} - \frac{C_F}{C_0} Q_{T,AV} + C_S V_{IN} \tag{4}$$

with P_{AV} and $Q_{T,AV}$ being the average spontaneous polarization and average trapped charge, respectively. By differentiating in time Eq. (4), we obtain the total current at the MF terminal, which is composed of

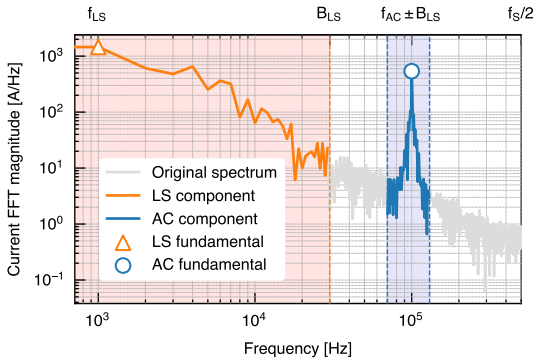

Figure 10: Spectrum of I_{FTJ} in Fig. 9b (gray). The LS (orange) and AC (blue) components have been extracted via ideal filters. The B_{LS} bandwidth is empirically chosen as $30 \times f_{LS}$. The sharp peak at f_{AC} and the AM-modulation behavior of I_{AC} in Fig. 9c support the extraction of the AC component of I_{FTJ} through a band-pass filter with $2B_{LS}$ bandwidth centered around f_{AC} (blue circle).

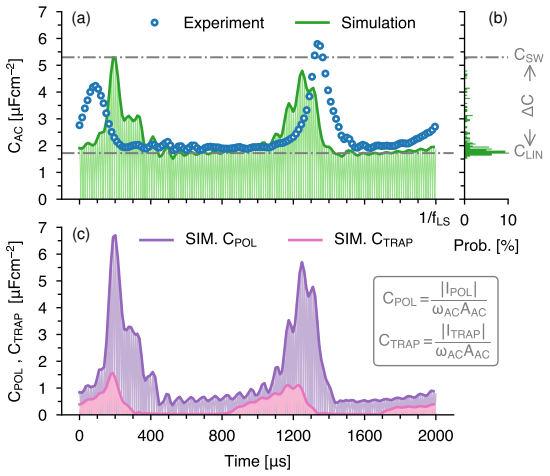

Figure 11: Simulations reproducing the new experimental technique, both performed at $f_{LS} = 500\,\text{Hz}$ and $f_{AC} = 40\,\text{kHz}$: (a) Comparison between the envelope of experimental C_{AC} (symbols) and the simulated C_{AC} (line). (b) Probability histogram of the simulated C_{AC} envelope of (a) used to extract C_{LIN}, C_{SW} and ΔC. (c) The HZO polarization contribution (C_{POL}) dominates in the overall C_{AC}, while the trap contribution (C_{TRAP}) is much lower.

three terms:

$$I_{MF} = I_{POL} + I_{TRAP} + I_{CS} \tag{5}$$

I_{POL}, I_{TRAP} and I_{CS} are the contribution of P_{AV}, $Q_{T,AV}$ and C_S to the displacement current, respectively. Then, as in the experiments, we can obtain the corresponding capacitances as $C_x = |I_x|/(2\pi f_{AC} A_{AC})$, where x stands for POL, $TRAP$ and CS. Figure 11c compares the simulated C_{POL} and C_{TRAP}: despite the fundamental role of traps in the stabilization of the HZO polarization [15], the trap contribution to C_{AC} appears negligible w.r.t. that of the ferroelectric, which is thus responsible for the C_{AC} peaks. This holds for all the simulated f_{LS} and f_{AC} values.

We drew the probability histograms of the capacitance in Figs. 9e, 9g and 11b to extract C_{LIN}, the

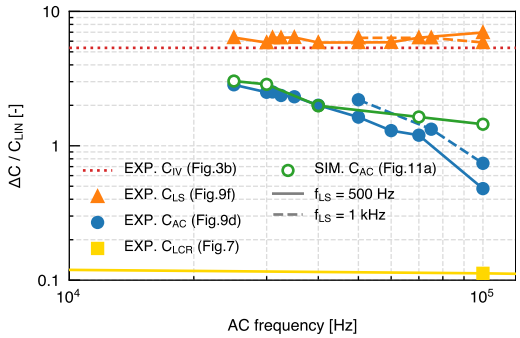

Figure 12: Experimental (full symbols) and simulated (open symbols) $\Delta C/C_{LIN}$ of the AC and LS capacitances vs. f_{AC} and for two f_{LS} values. Data for LCR experiments (yellow) and standard IV measurements (red) are also reported as a reference. $\Delta C/C_{LIN}$ of C_{AC} (blue circles) reduces for increasing f_{AC}. Such behavior is reproduced by the model, while it is not seen in LCR measurements.

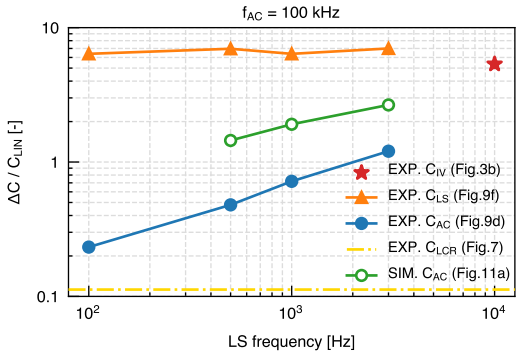

Figure 13: Experimental (full symbols) and simulated (green) $\Delta C/C_{LIN}$ of the AC and LS capacitance versus f_{LS} at fixed $f_{AC} = 100\,\text{kHz}$. LCR data (yellow, Fig. 7) and that from C_{IV} (red, Fig. 3b) are also reported as a reference. C_{AC} peaks increase with increasing f_{LS}. The model qualitatively reproduces the experimental trend.

peak capacitance C_{SW} and their difference ΔC, aiming to monitor the irreversible switching contribution to the calculated capacitances. Figure 12 shows $\Delta C/C_{LIN}$, hence the relative difference between C_{SW} and C_{LIN}, as a function of f_{AC} and for a couple of f_{LS} values. C_{LS} peak amplitudes agree well with those of C_{IV} in Fig. 3b, independently of f_{AC}. Instead, C_{AC} peaks lie between a minimum set by C_{LCR} in Fig. 7 and a maximum set by C_{IV} and they reduce with increasing f_{AC}, thus indicating a progressively smaller contribution of the irreversible switching at high f_{AC}. Simulations are in fairly good agreement with the experiments, while LCR meter experiments do not show at all this trend (Fig. 7).

In Fig. 12 the C_{AC} peaks increase with f_{LS}, so in Fig. 13 we report $\Delta C/C_{LIN}$ vs. f_{LS} for a $f_{AC} = 100\,\text{kHz}$. At low f_{LS}, $\Delta C/C_{LIN}$ of C_{AC} approaches the C_{LCR} reference, while at large f_{LS} it tends towards the C_{IV} data (red star). Also the model confirms this general trend. Hence, for the first time, these experiments provide a bridge between capacitance values measured through LS characterization or AC analysis. Figure 14 summarizes all the data measured for the different f_{LS} and f_{AC} values.

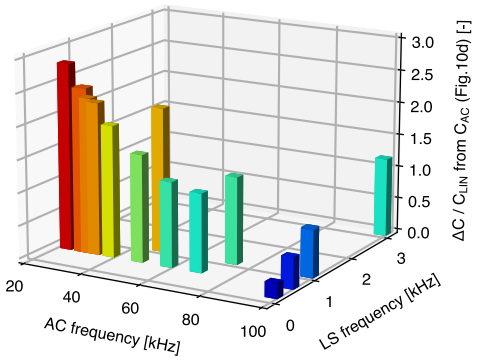

Figure 14: Summary of all the $\Delta C/C_{LIN}$ obtained from experimental C_{AC} for various f_{LS} and f_{AC}. When f_{LS} and f_{AC} converge, the measured capacitance peaks due to HZO switching increase.

VI. Conclusion

A new setup and novel experiments are used to characterize FTJs from LS to AC regimes. Measurements highlighted that the contribution of FE switching to C_{AC} is negligible in standard AC experiments, but it largely grows if the underlying bias changes over time. This behavior has been confirmed also by simulations. This may originate from the FE destabilization induced by the LS sweep, which enables the polarization to respond to the AC signal. In LCR experiments, instead, the DC bias applied for a fairly long time before the AC measurement stabilizes the FE polarization almost completely, thus dampening the polarization response to the AC stimulus (Fig. 5b).

The dependence of the C_{AC} peaks on f_{AC}, instead, may be explained by invoking the time constants related to irreversible polarization switching. Again, this trend is not observed in LCR experiments, since the contribution of irreversible polarization switching to C_{LCR} is negligible.

Acknowledgements

This work was supported by the European Union through the BeFerroSynaptic project (GA:871737).

References

[1] S. Slesazeck and T. Mikolajick, "Nanoscale resistive switching memory devices: a review," *Nanotechnology*, vol. 30, no. 35, p. 352003, jun 2019, DOI: 10.1088/1361-6528/ab2084.

[2] R. Fontanini, M. Segatto, K. S. Nair *et al.*, "Charge-Trapping-Induced Compensation of the Ferroelectric Polarization in FTJs: Optimal Conditions for a Synaptic Device Operation," *IEEE Transactions on Electron Devices*, vol. 69, no. 7, pp. 3694–3699, 2022, DOI: 10.1109/TED.2022.3175684.

[3] R. Fontanini, M. Segatto, M. Massarotto *et al.*, "Modeling and Design of FTJs as Multi-Level Low Energy Memristors for Neuromorphic Computing," *IEEE Journal of the Electron Devices Society*, vol. 9, pp. 1202–1209, 2021, DOI: 10.1109/JEDS.2021.3120200.

[4] S. Deng, Z. Jiang, S. Dutta *et al.*, "Examination of the Interplay Between Polarization Switching and Charge Trapping in Ferroelectric FET," in *2020 IEEE International Electron Devices Meeting (IEDM)*, 2020, pp. 4.4.1–4.4.4, DOI: 10.1109/IEDM13553.2020.9371999.

[5] K. Toprasertpong, M. Takenaka, and S. Takagi, "Direct Observation of Interface Charge Behaviors in FeFET by Quasi-Static Split C-V and Hall Techniques: Revealing FeFET Operation," in *2019 IEEE International Electron Devices Meeting (IEDM)*, 2019, pp. 23.7.1–23.7.4, DOI: 10.1109/IEDM19573.2019.8993664.

[6] J. Li, Y. Qu, M. Si *et al.*, "Multi-Probe Characterization of Ferroelectric/Dielectric Interface by C-V, P-V and Conductance Methods," in *2020 IEEE Symposium on VLSI Technology*, 2020, pp. 1–2, DOI: 10.1109/VLSITechnology18217.2020.9265069.

[7] Y. Qu, J. Li, M. Si *et al.*, "Quantitative Characterization of Interface Traps in Ferroelectric/Dielectric Stack Using Conductance Method," *IEEE Transactions on Electron Devices*, vol. 67, no. 12, pp. 5315–5321, 2020, DOI: 10.1109/TED.2020.3034564.

[8] M. Massarotto, F. Driussi, A. Affanni *et al.*, "Versatile experimental setup for FTJ characterization," *Solid-State Electronics*, vol. 194, p. 108364, 2022, DOI: 10.1016/j.sse.2022.108364.

[9] M. Massarotto, F. Driussi, A. Affanni *et al.*, "Novel experimental methodologies to reconcile large- and small-signal responses of Hafnium-based Ferroelectric Tunnel Junctions," *Solid-State Electronics*, vol. 200, p. 108569, 2023, DOI: 10.1016/j.sse.2022.108569.

[10] M. Segatto, R. Fontanini, F. Driussi *et al.*, "Limitations to Electrical Probing of Spontaneous Polarization in Ferroelectric-Dielectric Heterostructures," *IEEE Journal of the Electron Devices Society*, vol. 10, pp. 324–333, 2022, DOI: 10.1109/JEDS.2022.3164652.

[11] T. Rollo, F. Blanchini, G. Giordano *et al.*, "Stabilization of negative capacitance in ferroelectric capacitors with and without a metal interlayer," *Nanoscale*, vol. 12, pp. 6121–6129, 2020, DOI: 10.1039/C9NR09470A.

[12] H.-J. Lee, M. Lee, K. Lee *et al.*, "Scale-free ferroelectricity induced by flat phonon bands in HfO_2," *Science*, vol. 369, no. 6509, pp. 1343–1347, 2020, DOI: 10.1126/science.aba0067.

[13] M. Si, X. Lyu, P. R. Shrestha *et al.*, "Ultrafast measurements of polarization switching dynamics on ferroelectric and antiferroelectric hafnium zirconium oxide," *Applied Physics Letters*, vol. 115, no. 7, p. 072107, 2019, DOI: 10.1063/1.5098786.

[14] M. Segatto, M. Massarotto, S. Lancaster *et al.*, "Polarization switching and AC small-signal capacitance in Ferroelectric Tunnel Junctions," in *ESSDERC 2022 - IEEE 52nd European Solid-State Device Research Conference (ESSDERC)*, 2022, pp. 340–343, DOI: 10.1109/ESSDERC55479.2022.9947185.

[15] R. Fontanini, J. Barbot, M. Segatto *et al.*, "Interplay Between Charge Trapping and Polarization Switching in BEOL-Compatible Bilayer Ferroelectric Tunnel Junctions," *IEEE Journal of the Electron Devices Society*, vol. 10, pp. 593–599, 2022, DOI: 10.1109/JEDS.2022.3171217.